

Investigation of Nucleate Pool Boiling of Saturated Pure Liquids and Ethanol-Water Mixtures on Smooth and Laser-Textured Surfaces

Peter Zakšek, Matevž Zupančič, Peter Gregorčič & Iztok Golobič

To cite this article: Peter Zakšek, Matevž Zupančič, Peter Gregorčič & Iztok Golobič (2020) Investigation of Nucleate Pool Boiling of Saturated Pure Liquids and Ethanol-Water Mixtures on Smooth and Laser-Textured Surfaces, *Nanoscale and Microscale Thermophysical Engineering*, 24:1, 29-42, DOI: [10.1080/15567265.2019.1689590](https://doi.org/10.1080/15567265.2019.1689590)

To link to this article: <https://doi.org/10.1080/15567265.2019.1689590>

 View supplementary material [↗](#)

 Published online: 06 Nov 2019.

 Submit your article to this journal [↗](#)

 Article views: 146

 View related articles [↗](#)

 View Crossmark data [↗](#)

 Citing articles: 3 View citing articles [↗](#)



Investigation of Nucleate Pool Boiling of Saturated Pure Liquids and Ethanol-Water Mixtures on Smooth and Laser-Textured Surfaces

Peter Zakšek^a, Matevž Zupančič^{ib}, Peter Gregorčič^b, and Iztok Golobič^b

^aKrško Nuclear Power Plant, Vrblina, Krško, Slovenia; ^bFaculty of Mechanical Engineering, University of Ljubljana, Aškerčeva, Ljubljana, Slovenia

ABSTRACT

Nucleate pool boiling experiments were performed on plain and five laser-textured stainless-steel foils using saturated pure water, 100% ethanol, 0.4% and 4.2% mole fraction ethanol – water mixtures. All laser-textured samples contained untreated, smooth 0.5 mm wide regions and intermediate textured surfaces, that differ in the width of the laser patterned regions (from 0.5 mm to 2.5 mm). For smooth surfaces, we measured significant decreases in average heat transfer coefficients (HTC) and increases in bubble activation temperatures in comparison with the laser-textured surfaces for all the tested working fluids. Significant enhancement in HTC (280%) on a textured heating surface with 2.5-mm-wide laser pattern was recorded using pure water. For pure ethanol, the highest enhancement of 268% was achieved on a heating surface with 1.5-mm-wide laser pattern. The highest enhancement of HTC for the tested binary mixtures was obtained using 2.0-mm wide-laser-textured regions (HTC improved by 235% and 279% for the 0.4% and 4.2% mixtures, respectively). Our results indicate that laser texturing can significantly improve boiling performance when the intervals of the laser-textured patterns are close to the capillary lengths of the tested fluids.

ARTICLE HISTORY

Received 19 August 2019
Accepted 1 November 2019

KEYWORDS

Pool boiling; water; ethanol; binary mixtures; laser surface engineering; laser texturing; capillary length

Introduction

Nucleate pool boiling heat transfer has been intensively investigated with the intention of identification and improved understanding of the heat transfer mechanisms [1, 2]. A wide interest to gain a new knowledge about phase-change heat transfer with pure, single-component fluids and even more with binary mixture fluids systems arises from their wide use in a multitude of important processes, such as distillation, chemistry, petrochemistry, refrigeration, nuclear power generation etc [3–9]. Existing experimental results and many semi-empirical or theoretical models show that it is not easy to predict the boiling heat transfer coefficient even for single-component pure fluids [10–12]. Studies of boiling heat transfer with binary mixtures have demonstrated higher level of complexity, e.g., even the smallest amount of one of the two pure fluids in mixture leads to results, which cannot be predicted by simple linear interpolation between the heat transfer coefficients of the pure mixture components [3, 8, 13–15]. Different authors suggested various physical explanations for nonlinear reductions. They assumed a decrease of the individual effects during the boiling of mixtures: (i) local rise of the heater temperature due to preferred evaporation of more volatile component and resulting concentration gradients, (ii) limited mass diffusion of the more volatile

CONTACT Matevž Zupančič  matevz.zupancic@fs.uni-lj.si  Faculty of Mechanical Engineering, University of Ljubljana, Ljubljana, Slovenia

Color versions of one or more of the figures in the article can be found online at www.tandfonline.com/umte.

 Supplemental data for this article can be accessed [publisher's website](#).

components toward micro-layer on the way to nucleation site, and (iii) the effects of mixture physical properties on the nucleation phenomena [16–20].

The pioneering research work on boiling of binary mixtures began with Stephan and Körner [21]. They recognized that the absolute value of the difference between the mixture's more volatile component vapor and liquid molar concentrations causes a reduction of heat transfer intensity with binary mixtures. A number of later investigators (Clus and Leonidopoulos [22], Jungnickel et al. [23], Thome [24], Fujita et al. [25], Kandlikar [3]) followed these findings and developed different models for better prediction of boiling heat transfer using binary mixtures. However, there is still no theoretical method enabling the prediction of the heat transfer coefficient of binary mixtures with satisfactory accuracy. Thus, it is still necessary to implement an experimental approach to investigate boiling heat transfer of such working fluids [15, 26, 27].

Most research of boiling with binary mixtures has been limited to the variation of only one of the following influencing parameters: (i) the properties of the working fluid [28, 29] or (ii) the properties of the heater surface [30, 31]. Changing properties of the working fluid (e.g., using nano fluids) [32, 33], changing the physical conditions (e.g., pressure) [15] or changing of properties of the boiling surface (e.g., surface modification) [34, 35] can augment the boiling heat transfer. Due to the operating limits during the use of boiling in engineering applications, the preferred method is modification of the boiling surface [19]. Biao Shen et al. [36] studied pool boiling of ethanol on wettability-patterned surfaces. A polished copper surface was treated with an array of circular spots of a hydrophobic coating. They found that the maximal enhancement of the heat transfer coefficient is over 300% compared to a plain copper surface using a pitch-to-spot-ratio close to 2.5 mm. Sahu et al. [37] investigated pool boiling of ethanol, water and their binary mixtures on smooth and nano-textured surfaces comprised of copper-plated nanofibers. They found that the heat transfer coefficient is significantly higher at lower superheats when comparing nano-textured surfaces with smooth samples. The effect of bare copper and nano-textured surfaces was experimentally studied during the pool boiling of ethanol and self-wetting fluids by Sankaran [38], who found that 0.1 volume concentration of n-heptanol in an aqueous solution improved boiling heat transfer considerably. Rahman et al. [39] observed enhanced boiling heat transfer using surfaces by incorporating the low-conductivity materials at the interface between the surface and fluid. They manufactured an array of non-conductive lines incorporated into a high-conductive substrate. Spatial variation of the non-conductive lines with a capillary-length spacing showed an increase of HTC for more than five times. Voglar et al. [40] tested pool boiling performance of water on surfaces with the capillary-length-spaced one- and two-dimensional laser-textured patterns. They found the heater surfaces with hexagonally arranged textured circular shapes with a diameter of 2.0 mm in separated by capillary length for water (2.5 mm) provided a more than four times higher heat transfer coefficient compared to the untreated sample. Their experimental results showed that the spacing between treated and untreated areas of the surface should be equal to the capillary length of water.

In this study, we investigate the pool boiling performance of pure water, pure ethanol, and two ethanol – water mixtures (0.4% and 4.2%) on smooth and laser-textured stainless steel foils. Textured surfaces have parallel linear patterns of active nucleation sites spaced to cover the capillary lengths of both pure liquids (e.g., water and ethanol). Implementation of high-speed IR thermography in the boiling experiments allowed us to directly measure the transient temperature fields of the boiling surfaces in order to gain a detailed insight into the complex boiling phenomenon.

Materials and methods

Laser processing of the boiling surfaces

We recently proposed a cost-effective and chemical-free laser texturing process to produce surfaces for enhanced pool boiling heat transfer on metal substrates [35, 41]. Pulsed fiber laser (wavelength of 1060 nm, SPI Lasers Ltd., G4, SP-020P-A-HS-S-A-Y) with a pulse duration of 28 ns, pulse energy of

60 μJ , repetition rate of 25 kHz and beam waist diameter of 38 μm is led over the foil surface with a scanning velocity of 0.15 ms^{-1} . In this way, the 35- μm -wide microchannels, surrounded by remolten material on both sides, are produced. The distance between the microchannels is alternated between 40 μm , 45 μm and 50 μm (Figure 1d). This results in the appearance of multiscale microcavities on the borders between successive channels, as explained in Ref [41]. The diameters of laser-induced microcavities range from 0.2 μm to up to 10 μm , as presented in Figure 1e. According to the Hsu's nucleation criterion [35, 42] and considering that the contact angle of water on the laser textured surface is around 15°, the developed cavity diameters corresponds with the optimal cavity sizes for potentially active nucleation sites during saturated boiling of water.

Surface roughness of smooth (non-processed) and laser-textured regions were measured with an optical confocal microscope Alicona InfiniteFocus at 50x magnification (see Fig. S5). Analysis showed an average height value Sa of 0.16 μm and 2.2 μm for the smooth and the laser-textured region, respectively.

The boiling surfaces were designed with the notion of optimal spacing between the active nucleation sites for water and pure ethanol, which was set to the capillary lengths equal to 2.5 mm and 1.55 mm, respectively. On this basis, we created the laser-textured lines that were separated by 0.5-mm-wide untreated areas in the y direction throughout the entire surface (Figure 1c). The period P of the laser-textured lines was in the range of 1.0–3.0 mm. It is expected that multi-scale microcavities on each laser-textured line interval will present active nucleation sites, leading to the enhancement of the nucleation site density and improvement of the boiling performance. Coverage ratio for the laser-textured line intervals on each heating surfaces in comparison to the entire surface is shown in Table 1.

Preparation of the boiling fluids

Double-distilled water (Roth, 3478) and ethanol (EMSURE ACS) were used as the working fluids. We tested pure water, ethanol of purity $\geq 99.9\%$, and ethanol-water mixtures with an ethanol mole

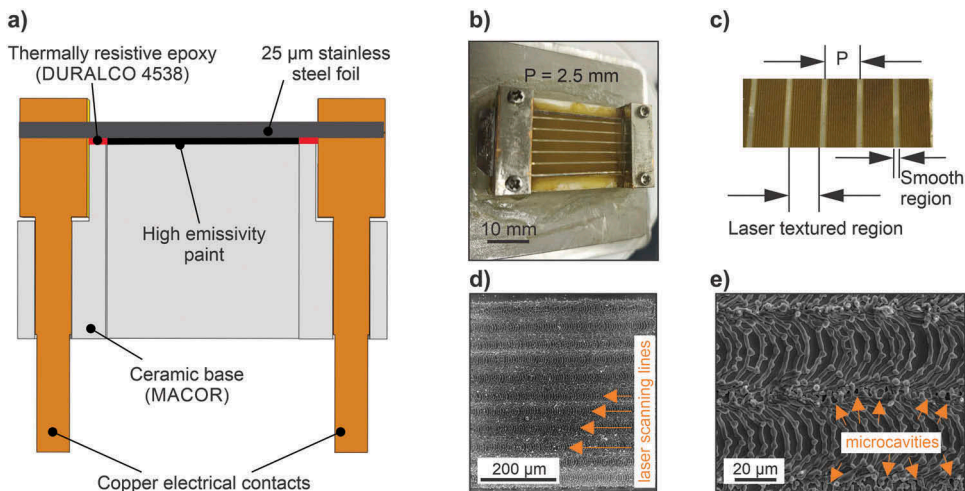


Figure 1. (a) Cross-section view of the thin metal foil heater unit; (b) a stainless steel foil with the 2.5 mm laser pattern width; (c) an optical image of the laser-textured foil; (d) SEM image of the laser-textured area; and (e) the magnified SEM image of the microcavities, which formed in between the laser scanning lines.

Table 1. Laser pattern widths and laser coverage ratio for all tested samples.

Laser pattern width [mm]	0.0 ^a	0.5	1.0	1.5	2.0	2.5
Period P [mm]	0 ^a	1.0	1.5	2.0	2.5	3.0
Laser area coverage of boiling surface [%]	0 ^a	50	65	74	79	82

^asmooth untreated stainless steel sample

Table 2. Properties of pure fluids and ethanol-water mixtures.

Mole fraction of ethanol-water mixture χ [%]	Molar mass M [g/mol]	Boiling point [°C at 1013 hPa]	Capillary length λ_c [mm]
0	18.01	100	2.5
0.4	18.12	98.8	2.4
4.2	19.18	91.2	2.3
100	46.07	78.3	1.55

fraction of 0.4% and 4%, respectively. Properties of the used fluids shown in Table 2 were acquired using REFPROP software [43] and their capillary length was determined by Equation (1).

$$\lambda_c = \sqrt{\frac{\gamma}{(\rho_l - \rho_v)g}} \quad (1)$$

Pool boiling experiments

A detailed explanation of the experimental system, the method for determining the distribution of the local heat fluxes and the measurement uncertainty are reported in our previous work [16, 35, 44] as well as in the Supplementary material. Pool boiling experimental setup consists of a boiling chamber, power supply unit, data acquisition system and high-speed visualization system (see Figure S3). Boiling chamber with external dimensions of $170 \times 100 \times 100 \text{ mm}^3$ is made of two steel plates and walls made of double-pane glass to enable visualization and at the same time minimize heat losses during the measurements. The heater unit (schematically presented in Figure 1a) with 25- μm stainless steel foil (S316, Precision Brand; effective boiling area of $17 \times 27 \text{ mm}^2$) is mounted on the bottom of the boiling chamber. Stainless steel foils are powered with direct current (TDK Lambda, GEN 10–1000) and are, therefore, heated with the Joule effect. The heater unit has a rectangular borehole milled in the center to enable the IR thermographic observation of a thin foil from the bottom side, which is painted with a high-emissivity paint (emissivity of 0.90, thickness $< 2 \mu\text{m}$) in order to improve the accuracy of the IR measurements.

Water, ethanol and ethanol-water mixtures were boiled for 2 h prior to the experiments in order to remove dissolved gasses. An immersed cartridge heater is used for degassing, preheating and maintaining the saturation temperature during the experiments. Bulk temperature is measured with two K-type thermocouples (placed at the same level as the boiling surface and 0.5 cm below the liquid level). Vapor temperature is measured with one K-type thermocouple placed about 1.0 cm above the liquid level. Voltage and temperature signals are recorded with an Agilent 34970A data acquisition unit and a multiplexer module 34901A.

The visualization system consists of the high-speed IR camera (FLIR SC6000) recording at 1000 fps. Spatial resolution of the IR thermography equals 125 μm per pixel. For each given heat flux we acquired 10 s of recording. Thus, the IR measurement at a certain heat flux consists of 10,000 consecutive frames (10 s of recording at 1000 fps), which corresponds to more than 10^8 individual temperature points considering the IR image resolution is at least 128×80 pixels. In addition to boiling curves that show spatio-temporal averaged heat flux versus wall superheat, we also report wall-temperature distributions in order to determine variation of the wall temperatures at certain operating conditions. Calculation of the wall-temperature distributions is discussed in details in our previous publication [44], whereas the calculation of local heat fluxes is provided by equations (S9) and (S10) in the Supplementary material.

The transient temperature fields, measured from the bottom, directly depend on the boiling process that takes place on the upper side of the electrically heated foils. The effects of vertical and lateral heat conduction as well as the response of the heater to the periodic temperature disturbance are quantified in the Supplementary material (see Figs. S2–S4). Overall, the absolute temperature-measurement uncertainty is 2 K and the noise equivalent differential temperature (i.e., sensitivity) of

the IR camera is 20 mK. Relative uncertainty of the measured heat flux was estimated as 0.5% and the maximum expanded uncertainty of the heat transfer coefficient equals 3.5 kW/m²K.

Results and discussion

Boiling curves

The measured boiling curves for different working fluids are shown in Figure 2. Smooth surfaces are represented with a five-pointed star (pentagram), while other symbols are used for the laser-textured surfaces. If we only consider heat fluxes greater than 75 kW/m², where the nucleate boiling was fully developed, we can observe that the entire laser-textured surfaces provide on average significantly lower superheats (7.8 K, 6.3 K, 8.2 K and 8.9 K) than the smooth sample for all of the tested working fluids. Heating surface with 2.5 mm wide laser patterns provides the most effective heat transfer with pure water with the lowest superheat over the entire measuring range. For pure ethanol, the optimal heating surface is treated using a laser pattern with a width of 1.5 mm. For 0.4% and 4.2% ethanol-water mixtures, the surface with 2.0 mm texturing width provides the best heat transfer coefficient.

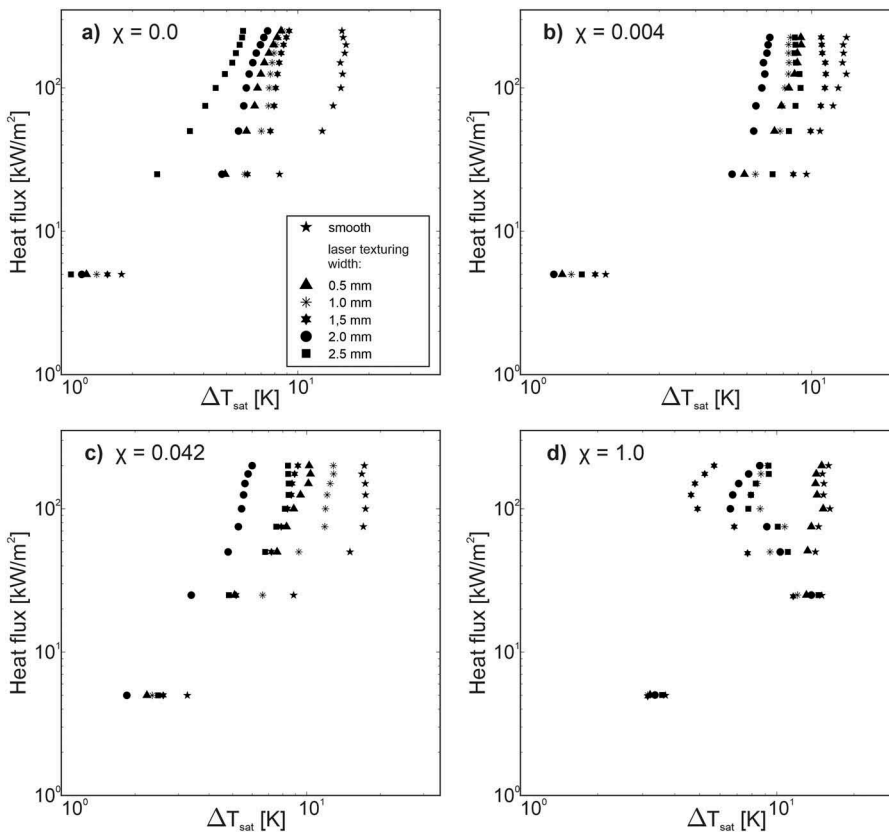


Figure 2. Boiling curves for all the surfaces and for each of the tested working fluid: (a) pure water, (b) 0.4% ethanol-water mixture, (c) 4.2% mixture, and (d) pure ethanol.

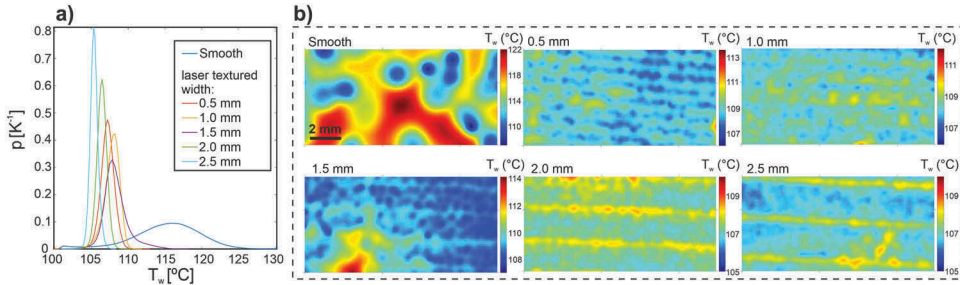


Figure 3. Saturated pool boiling of water at 250 kW/m^2 : (a) wall-temperature distributions and (b) time-averaged temperature fields.

Wall-temperature distributions and time-averaged wall temperature fields

To explain the differences in boiling performance between smooth and laser-textured surfaces, we further analyzed IR recordings at different heat fluxes: water (up to 250 kW/m^2 in Figure 3), 0.4% ethanol-water mixture (up to 225 kW/m^2 in Figure 4), 4.2% ethanol-water mixture (up to 200 kW/m^2 in Figure 5), and pure ethanol (up to 150 kW/m^2 in Figure 6). Figures 3–6 show the wall-temperature distributions as well as the temperature fields for different boiling surfaces. Note that x -axis in Figures 3–6(a) represents the absolute wall temperature and that saturation temperatures equal 100°C , 98.8°C , 91.2°C and 78.3°C for water, 0.4% and 4.2% ethanol-water mixtures, and pure ethanol, respectively. Average temperature fields are calculated based on 10 s of recording at 1000 fps. Thus, each pixel value in Figures 3–6(b) represents the 10-s temperature average. The cold spots on the time-averaged temperature fields coincide with the active nucleation sites during boiling.

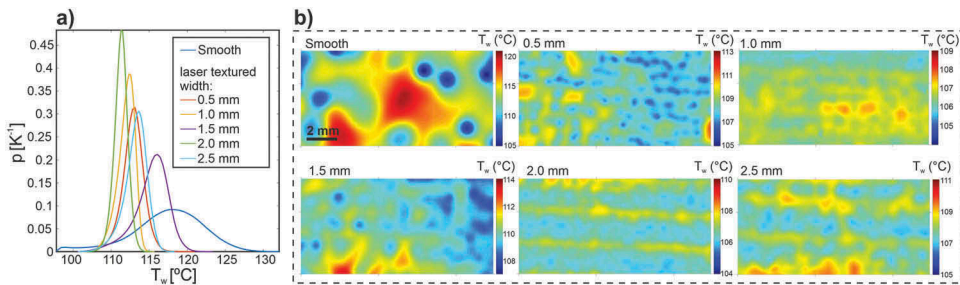


Figure 4. Saturated pool boiling of 0.4% ethanol-water mixture at 225 kW/m^2 : (a) wall-temperature distributions and (b) time-averaged temperature fields.

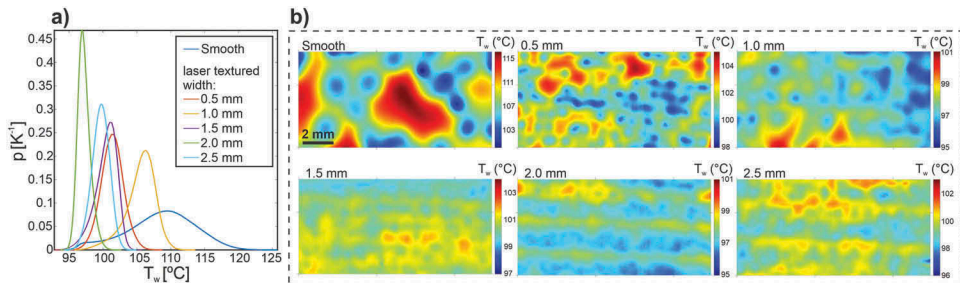


Figure 5. Saturated pool boiling of 4.2% at 200 kW/m^2 : (a) wall-temperature distributions and (b) time-averaged temperature fields.

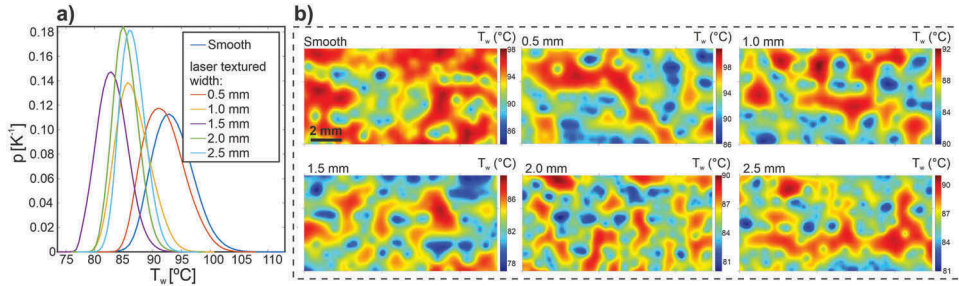


Figure 6. Saturated pool boiling of pure ethanol at 150 kW/m^2 : (a) wall-temperature distributions and (b) time-averaged temperature fields.

It is clear from [Figure 3a](#) that the peaks of the distributions of wall temperatures are significantly higher on the laser-textured surfaces compared to the smooth sample and the maximal values of the temperatures are much lower during boiling on laser-textured surfaces. The most significant difference is observed on the laser-textured surfaces with 2.5-mm-wide textured regions. The standard deviation on the laser-textured surfaces is on average 11 K lower compared to the temperature standard deviation on the smooth surface. For water at 250 kW/m^2 , a local maximum temperature of 128°C was measured on the smooth surface, while the maximum reached only 107.5°C on the laser-textured surface. Average temperature fields in [Figure 3b](#) reveal that active nucleation sites are randomly distributed on the smooth surface, while on the laser-textured surface virtually each structured region represents an active nucleation region (e.g., see boiling of water at 250 kW/m^2). This results in a more discrete temperature pattern across the entire foil, where the laser-induced multiscale microcavities also provide lower bubble activation temperatures. From the thermograms, it also follows that the laser-textured areas limit the bubble contact diameter and prevent horizontal coalescence directly on the boiling surface. Since boiling does not take place on smooth regions, the coalescence is partially prevented only perpendicularly to the laser scanning lines (e.g. across the smooth surface regions).

Results for 0.4% and 4.2% ethanol-water mixtures at 225 kW/m^2 and 200 kW/m^2 are shown on [Figures 4.5](#). Again, one can observe that each detected nucleation site corresponds with the location of the laser-textured lines. The calculated capillary length (2.4 mm) for 0.4% ethanol-water mixture is only 0.1 mm away from the 2.5-mm-laser-patterned width and it is far closer as the next nearest laser-patterned interval of 2.0 mm. On this basis, one expects the best performance on the same sample as with water. However, only a small amount of ethanol (0.4% ethanol-water mixture) causes a major influence on the boiling heat transfer. The standard deviation of wall temperature is on average 3.2 K lower on 2.0 mm laser patterned width compared to the 2.5 mm width. Further results for the 4.2% ethanol-water mixture ([Figure 5](#)) with a capillary length of 2.3 mm show that the best boiling performance was achieved on the surface with pitch of the textured regions equal to 2.5 mm (laser-textured width of 2.0 mm). Standard deviation of the wall temperature in fully developed nucleate boiling regime is on average 3.6 K lower on 2.0 mm textured widths compared to 2.5 mm. Additionally, the surface with 2.0-mm-wide texturing provides on average 12.6 K lower standard deviation than the smooth surface.

Using pure ethanol, one can observe that the highest heat transfer coefficient is achieved on the surface with 1.5-mm-wide laser-textured areas. On the one hand, the surface with 1.5-mm-wide areas provides the lowest bubble activation temperatures and average wall superheat, while on the other hand, optimally distributed nucleation sites provide lower maximum temperatures compared to all other surfaces. Compared to the smooth foil at 150 kW/m^2 , the local maximum temperature on the 1.5-mm-wide textured surface is 13.2 K lower. With pure ethanol, it is not able to clearly distinguish between the textured areas (boiling regions) and the smooth areas (non-boiling regions)

based on the thermograms (Figure 6b). This is due to much lower heat of vaporization of ethanol (849.6 kJ/kg) compared to water (2256.5 kJ/kg). Consequently, each individual bubble causes a smaller temperature drop during the nucleation, which is harder to detect. Taking into account the differences in bubble size between ethanol and water, we are not able to clearly capture each nucleation event, despite the fact we used thin (25- μm) stainless steel foils. To clearly identify each nucleation, even for the smallest ethanol bubbles, it would require a setup with even thinner foils or thin metal films atop of IR transparent glass. Despite this, we are able to measure average wall superheat (within a given measurement uncertainty) and show that the surface with 1.5-mm-wide textured areas in this case provides the highest heat transfer coefficient across the entire range of the measured heat fluxes.

Average heat transfer coefficients

Average heat transfer coefficients for the heat fluxes from 50 kW/m^2 (increasing steps of 25 kW/m^2) for all of the used working fluids are shown on Figure 7. Laser-textured surfaces promote heat transfer coefficient and minimize the superheat for each measured fluid, regardless of the pitch between the laser-textured regions. The highest heat transfer coefficient for pure working fluids (34.6 $\text{kW/m}^2\text{K}$ for water at 250 kW/m^2 and 23.8 $\text{kW/m}^2\text{K}$ for ethanol at 150 kW/m^2) was observed on laser-textured surfaces with the widths of the textured area corresponding to the distance of the

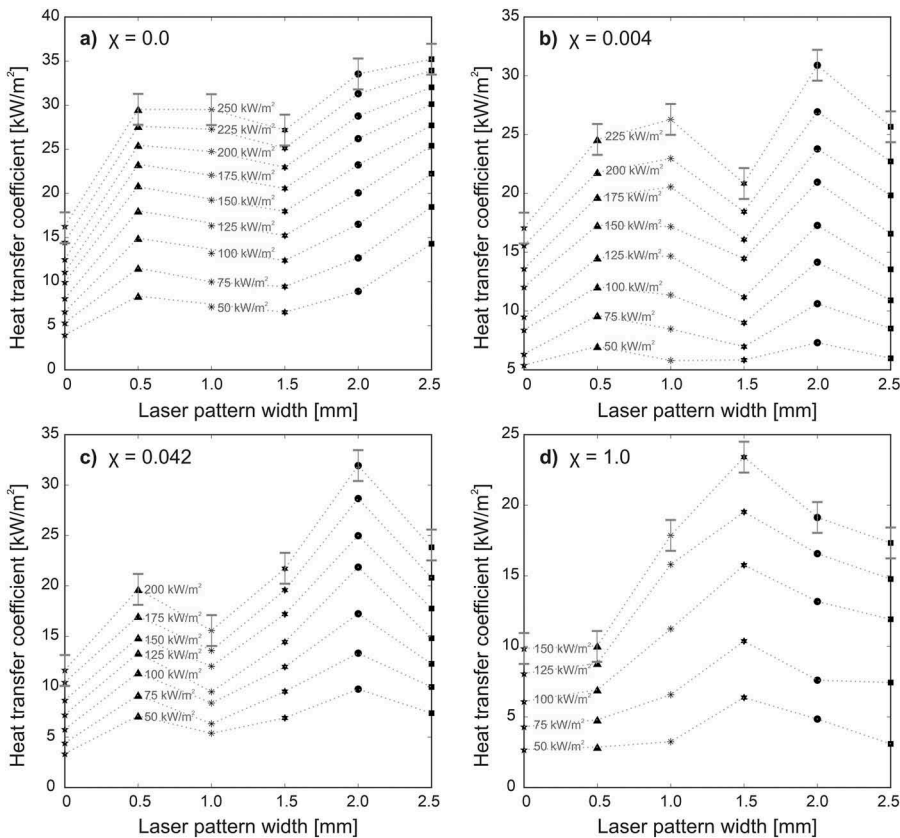


Figure 7. Average heat transfer coefficients for (a) pure water, (b) 0.4% ethanol-water mixture, (c) 4.2% mixture and (d) pure ethanol at different widths of laser-textured regions. For the sake of clarity, standard measurement uncertainty of heat transfer coefficient is only shown for the highest heat flux.

capillary length. The optimal spacing between the laser pattern intervals for ethanol-water mixtures is between the capillary lengths of pure substances. Results for both ethanol-water mixtures exhibited the highest heat transfer coefficients on 2.0-mm-wide texturing. At 200 kW/m², heat transfer coefficient of 26.8 kW/m²K was measured during boiling of 0.4% ethanol-water mixture and 31.7 kW/m²K for the 4.2% mixture.

The HTC enhancement factor on the laser-textured surfaces in comparison with the smooth, reference foil is shown in Table 3. The calculated capillary length [Equation (1)] for pure water and pure ethanol at the saturation temperature equals 2.5 mm, and 1.55 mm, respectively. This correlates with peaks of HTC enhancement factor for pure fluids (regarding the widths of the textured areas). Surface with the 2.0-mm-wide texturing regions has peaks of HTC enhancement factor at 2.35 for 0.4% and 2.79 for 4.2% mixture, respectively. Except for pure ethanol on 0.5 mm surface, the heat transfer coefficient is enhanced for more than 50% on the laser-textured surfaces for all of the tested fluids.

Local heat flux distributions

To better explain the distribution of the active nucleation sites and the optimal pattern design for a given fluid, we used the temperature fields to calculate a local heat flux distribution based on the equations explained in ref [12]. Figure 8 represents the time-averaged heat flux distribution (at nominal heat flux of 150 kW/m²) for 0.4% ethanol-water mixture. On the left-hand side of Figure 8, each circular region with a higher local heat flux represents an active nucleation site, whereas the diameter of this region corresponds to the bubble footprint diameter during its growth.

On the surface with the 1.5 mm laser pattern width (Figure 8a), we can observe that a single nucleation site is formed across the width of the laser-textured area, as schematically shown on the right-hand side of Figure 8. Untreated areas represent the regions of low heat flux, implying that no boiling takes place on those areas. In this case, the bubble footprints have an average diameter of 0.7 mm. When the laser-textured width is increased to 2.0 mm (Figure 8b), several nucleation sites are observed across the width of the textured area and the bubble footprints are decreased to approximately 0.4 mm. Consequently, nucleation site density is increased from 20 sites/cm² (for 1.5 mm surface) to 63 sites/cm² (for 2.0 mm surface), which reflects in the increased heat transfer coefficient, as represented in Figure 7b and Table 3. Additional increase in the laser-textured width to 2.5 mm then reduces the nucleation site density and increases the bubble footprint diameter (decreasing the nucleation frequency), which corresponds to a decrease of the heat transfer coefficient.

The results in Figure 7 show that by changing the width of the laser-textured area, the peak of the heat transfer coefficient is achieved for all the tested fluid mixtures. However, the comparison of the results in Figure 7 with the data in Table 2 show that this peak is achieved at periods larger than the capillarity length. Note that the period equals to the sum of the width of the textured area (x -axis of graphs on Figure 7) and the width of the non-treated surface (0.5 mm in our case).

This imply that the existing capillary-length criteria can be used (only) as a guideline in development of surfaces with optimally arranged patterns of active (boiling preferential) and non-active (non-boiling) regions – not only for water, but also for ethanol and ethanol-water mixtures, which has not been shown before. Despite the agreement with the results from other

Table 3. The HTC enhancement factor at 150 kW/m².

Laser pattern width	0 mm	0.5 mm	1.0 mm	1.5 mm	2.0 mm	2.5 mm
Water	1	2.09	1.94	1.81	2.34	2.80
0.4%	1	1.93	2.15	1.51	2.35	2.00
4.2%	1	1.70	2.18	1.63	2.79	1.92
100% Ethanol	1	1.12	1.82	2.68	2.15	1.84

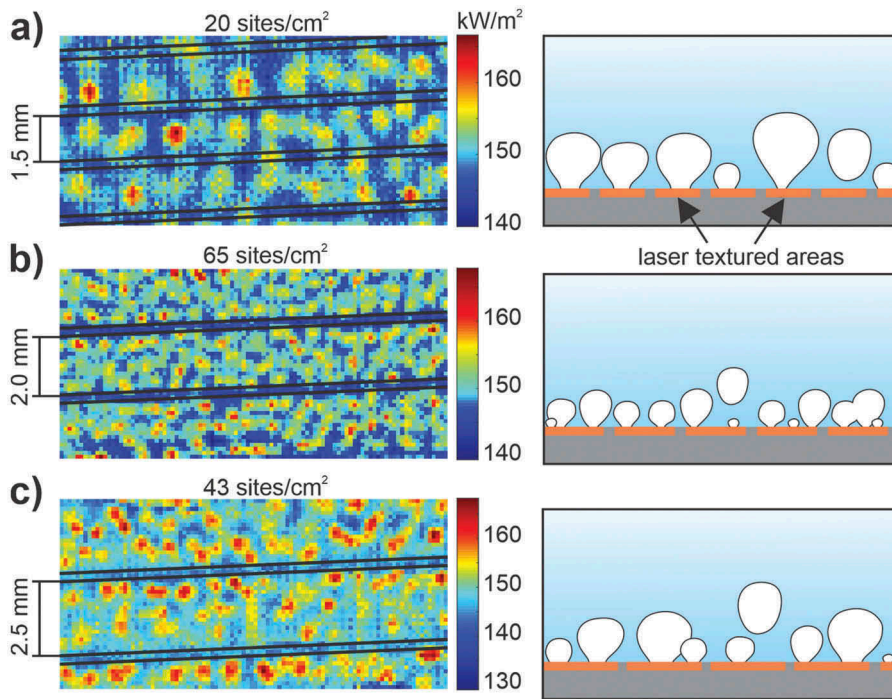


Figure 8. The time-averaged heat flux distribution at nominal heat flux of 150 kW/m^2 and interpretation of the bubble distribution for 0.4% ethanol-water mixture on surfaces with (a) 1.5 mm, (b) 2.0 mm and (c) 2.5 mm laser pattern widths. On the left-hand side, the 0.5-mm-wide untreated areas are marked with the black parallel lines.

investigations [39, 40], the high-speed IR measurement of the boiling surface revealed new and important insights.

The idea to create separate liquid return pathways in the non-active areas with the wavelength (P) corresponding to the expected bubble size, should provide the highest heat transfer coefficient. In this configuration, the bubbles would ideally form in the middle of the active boiling area and their lateral coalescence would be prevented due to the intermediate non-active areas, as observed in Figure 8a. However, slightly larger laser-textured area (Figure 8b) allows multiple nucleation sites across the laser-textured width, which significantly increases the nucleation site density and increases the heat transfer coefficient across a wide range of heat fluxes, despite the higher probability of lateral bubble coalescence. This shows that the capillary length criteria are not the ultimate optimization technique for all types of surface/fluid pairs. Rather, the optimum should be determined based on the maximization of the nucleation site density [45], while allowing the liquid to replenish active nucleation sites to avoid the dry-out event.

Conclusions

Saturated pool boiling investigation was carried out using water, ethanol and two different ethanol-water mixtures with heat fluxes from 50 kW/m^2 to up to 250 kW/m^2 . Nucleate pool boiling heat transfer coefficients were measured on the untreated and laser-textured stainless steel foils. Results show that laser texturing improves nucleate pool boiling performance not only for pure fluids, which has been already shown, but also for binary mixtures of water and ethanol.

The improvement results due to the formation of microcavities that act as active nucleation sites. This increases the nucleation site density and nucleation frequency and lowers the temperature of onset of nucleate boiling. Also, in case of binary mixtures, the multiscale microcavities with appropriate dimensions effectively trap vapor and provide spots for bubble growth. Thus, our results show that the laser texturing of surfaces has a potential to improve applications of distillation processes.

The most important result of this work is the optimization of the laser-patterned width between the untreated smooth regions. Results lead to the conclusion that a peak in the heat transfer coefficient can be obtained by changing the width of the laser-textured areas. In designing the pattern of the surface, the capillary length criteria of active/non-active areas could give a good starting point in maximizing the heat transfer coefficient not only for pure fluids, but also for various types of mixtures. However, the true maximization of the boiling performance was in our case always achieved on the surfaces that provided the highest nucleation site density. Additionally, the period (P) between the active and non-active areas does not necessarily completely agree with the capillary length of the working fluid. In our case, this period was always (i.e., for all the tested fluids) above the capillary length.

The highest measured heat flux coefficient of $34.6 \text{ kW/m}^2\text{K}$ (at a heat flux of 250 kW/m^2) for water was achieved on a laser-textured surface with 2.5-mm-wide regions separated by 0.5-mm-interruptions. Compared to the smooth, untreated sample the improvement equaled 280%. A similar improvement (268%) was measured also for pure ethanol. However, in this case, the highest improvement was achieved on the sample with 1.5-mm-wide laser-textured region (period of 2.0 mm). For the tested ethanol-water mixtures, the highest enhancement of the heat transfer coefficient was obtained using 2.0-mm-wide laser-textured regions (for 0.4% mixture it equaled $26.8 \text{ kW/m}^2\text{K}$ at 225 kW/m^2 , while for 4.2% mixture it equaled $31.7 \text{ kW/m}^2\text{K}$ at 200 kW/m^2). Overall, the laser texturing with multiscale microcavities lead to an enhancement of the heat transfer coefficient over the entire range of heat fluxes.

Highlights

- Study presents boiling of water and ethanol-water mixtures on laser-textured foils.
- Pulsed fiber laser was used to create active and non-active boiling regions.
- High-speed IR thermography was used to measure transient temperature fields.
- Laser-made microcavities provide active nucleation sites on all tested fluids.
- Boiling patterns close to the fluids' capillary length show the best performance.

Acknowledgments

The authors acknowledge the financial support from the state budget by the Slovenian Research Agency (research core funding No. P2-0223 and P2-0392 and project No. J2-1741). The authors would also like to thank SPI Lasers Ltd. for their support of the research project *Surface functionalization by nanosecond fiber laser texturing* (nsFLaT) and Dr. Matej Hočevar from the Institute of metals and technology (Slovenia) for providing SEM images and 3D surface measurements.

Declaration of interest

The authors declare no competing financial interest.

Funding

This work was supported by the Javna Agencija za Raziskovalno Dejavnost RS [J2-1741,P2-0223,P2-0392].

Nomenclature

M	molar mass (g/mol)
P	wavelength (m)
\dot{q}	heat flux (W/m^2)
T	temperature (K or $^{\circ}\text{C}$)
p	probability density (1/K)
g	acceleration of gravity (m^2/s)
fps	frames per second (1/s)

Greek symbols

α	HTC; heat transfer coefficient ($\text{W}/\text{m}^2\text{K}$)
λ_c	capillary length (m)
χ	mole fraction ethanol-water mixtures; (/or %)
Δ	delta
ρ	density (kg/m^3)
γ	liquid surface tension (N/m)

Subscript

w	wall
l	liquid
v	vapor

ORCID

Matevž Zupančič  <http://orcid.org/0000-0003-3411-7752>

References

- [1] J. Kim, “Review of nucleate pool boiling bubble heat transfer mechanisms,” *Int. J. Multiphase Flow*, vol. 35, pp. 1067–1076, 2009. DOI: [10.1016/j.ijmultiphaseflow.2009.07.008](https://doi.org/10.1016/j.ijmultiphaseflow.2009.07.008).
- [2] S. J. D. Van Stralen, “The mechanism of nucleate boiling in pure liquids and in binary mixtures—part I,” *Int. J. Heat Mass Transfer*, vol. 9, pp. 995–1020, 1966. DOI: [10.1016/0017-9310\(66\)90025-1](https://doi.org/10.1016/0017-9310(66)90025-1).
- [3] S. G. Kandlikar, “Boiling heat transfer with binary mixtures: part I—A theoretical model for pool boiling,” *J. Heat Transfer*, vol. 120, pp. 380–387, 1998. DOI: [10.1115/1.2824260](https://doi.org/10.1115/1.2824260).
- [4] A. Surtaev, V. Serdyukov, J. Zhou, A. Pavlenko, and V. Tumanov, “An experimental study of vapor bubbles dynamics at water and ethanol pool boiling at low and high heat fluxes,” *Int. J. Heat Mass Transfer*, vol. 126, pp. 297–311, 2018. DOI: [10.1016/j.ijheatmasstransfer.2018.06.001](https://doi.org/10.1016/j.ijheatmasstransfer.2018.06.001).
- [5] R. Reddy and J. Lienhard, “The peak boiling heat flux in saturated ethanol–water mixtures,” *J. Heat Transfer*, vol. 111, pp. 480–486, 1989. DOI: [10.1115/1.3250702](https://doi.org/10.1115/1.3250702).
- [6] S. Sinha-Ray, *et al.*, “Swing-like pool boiling on nano-textured surfaces for microgravity applications related to cooling of high-power microelectronics,” *Npj Microgravity*, vol. 3, pp. 9, 2017. DOI: [10.1038/s41526-017-0014-z](https://doi.org/10.1038/s41526-017-0014-z).
- [7] C. Colin, *et al.* “Nucleate pool boiling in microgravity: recent progress and future prospects,” *C.R. Mec.*, vol. 345, pp. 21–34, 2017. DOI: [10.1016/j.crme.2016.10.004](https://doi.org/10.1016/j.crme.2016.10.004).
- [8] Y. L. Tzan and Y. M. Yang, “Pool boiling of binary mixtures,” *Chem. Eng. Commun.*, vol. 66, pp. 71–82, 1988. DOI: [10.1080/00986448808940261](https://doi.org/10.1080/00986448808940261).
- [9] L. Sargentini, M. Bucci, G. Su, J. Buongiorno, and T. McKrell, “Experimental and analytical study of exponential power excursion in plate-type fuel,” 2014 Am. Nucl. Soc. Embedded Topical Meeting Adv. Therm. Hydraulics (ATH 14), June 15–19, 2014.
- [10] W. Gao, J. Qi, X. Yang, J. Zhang, and D. Wu, “Experimental investigation on bubble departure diameter in pool boiling under sub-atmospheric pressure,” *Int. J. Heat Mass Transfer*, vol. 134, pp. 933–947, 2019. DOI: [10.1016/j.ijheatmasstransfer.2019.01.024](https://doi.org/10.1016/j.ijheatmasstransfer.2019.01.024).
- [11] A. Guion, S. Afkhami, S. Zaleski, and J. Buongiorno, “Simulations of microlayer formation in nucleate boiling,” *Int. J. Heat Mass Transfer*, vol. 127, pp. 1271–1284, 2018. DOI: [10.1016/j.ijheatmasstransfer.2018.06.041](https://doi.org/10.1016/j.ijheatmasstransfer.2018.06.041).

- [12] I. Golobic, J. Petkovsek, and D. B. R. Kenning, "Bubble growth and horizontal coalescence in saturated pool boiling on a titanium foil, investigated by high-speed IR thermography," *Int. J. Heat Mass Transfer*, vol. 55, pp. 1385–1402, 2012. DOI: [10.1016/j.ijheatmasstransfer.2011.08.021](https://doi.org/10.1016/j.ijheatmasstransfer.2011.08.021).
- [13] A. Sitar and I. Golobic, "Heat transfer enhancement of self-rewetting aqueous n-butanol solutions boiling in microchannels," *Int. J. Heat Mass Transfer*, vol. 81, pp. 198–206, 2015. DOI: [10.1016/j.ijheatmasstransfer.2014.10.034](https://doi.org/10.1016/j.ijheatmasstransfer.2014.10.034).
- [14] J. R. Thome, "Enhanced boiling of mixtures," *Chem. Eng. Sci.*, vol. 42, pp. 1909–1917, 1987. DOI: [10.1016/0009-2509\(87\)80137-9](https://doi.org/10.1016/0009-2509(87)80137-9).
- [15] Y. Fujita and M. Tsutsui, "Heat transfer in nucleate pool boiling of binary mixtures," *Int. J. Heat Mass Transfer*, vol. 37, pp. 291–302, 1994. DOI: [10.1016/0017-9310\(94\)90030-2](https://doi.org/10.1016/0017-9310(94)90030-2).
- [16] M. Zupančič, J. Voglar, P. Gregorčič, I. Golobič, and P. Zakšek, "Saturated nucleate pool boiling of ethanol-water binary mixtures on smooth and enhanced laser processed metal surfaces," *ASME 2018 16th Int. Conf. Nanochannels Microchannels Minichannels*, June 10–13, 2018.
- [17] S. A. Alavi Fazel, A. A. Safekordi, and M. Jamialahmadi, "Pool boiling heat transfer in water/amines solutions," *IJE Trans. Basics*, vol. 21, pp. 113–131, 2008.
- [18] S. A. Alavi Fazel and M. Jamialahmadi, "Semi-empirical modeling of pool boiling heat transfer in binary mixtures," *Int. J. Heat Fluid Flow*, vol. 44, pp. 468–477, 2013. DOI: [10.1016/j.ijheatfluidflow.2013.08.002](https://doi.org/10.1016/j.ijheatfluidflow.2013.08.002).
- [19] P. Gupta, M. Hayat, and R. Srivastava, "A review on nucleate pool boiling heat transfer of binary mixtures," *Asian J. Water Environ. Pollut.*, vol. 16, pp. 27–34, 2019. DOI: [10.3233/AJW190016](https://doi.org/10.3233/AJW190016).
- [20] C. Cai, H. Liu, X. Xi, M. Jia, and H. Yin, "Bubble growth model in uniformly superheated binary liquid mixture," *Int. J. Heat Mass Transfer*, vol. 127, pp. 629–638, 2018. DOI: [10.1016/j.ijheatmasstransfer.2018.07.084](https://doi.org/10.1016/j.ijheatmasstransfer.2018.07.084).
- [21] K. Stephan and M. Körner, "Berechnung des Wärmeübergangs verdampfender binärer Flüssigkeitsgemische," *Chem. Ing. Tech.*, vol. 41, pp. 409–417, 1969. DOI: [10.1002/cite.330410702](https://doi.org/10.1002/cite.330410702).
- [22] W. F. Calus and D. J. Leonidopoulos, "Pool boiling—binary liquid mixtures," *Int. J. Heat Mass Transfer*, vol. 17, pp. 249–256, 1974. DOI: [10.1016/0017-9310\(74\)90086-6](https://doi.org/10.1016/0017-9310(74)90086-6).
- [23] H. Jungnickel, P. Wassilew, and W. E. Kraus, "Investigations on the heat transfer of boiling binary refrigerant mixtures," *Int. J. Refrig.*, vol. 3, pp. 129–133, 1980. DOI: [10.1016/0140-7007\(80\)90092-4](https://doi.org/10.1016/0140-7007(80)90092-4).
- [24] J. R. Thome, "Prediction of binary mixture boiling heat transfer coefficients using only phase equilibrium data," *Int. J. Heat Mass Transfer*, vol. 26, pp. 965–974, 1983. DOI: [10.1016/S0017-9310\(83\)80121-5](https://doi.org/10.1016/S0017-9310(83)80121-5).
- [25] Y. Fujita and M. Tsutsui, "Heat transfer in nucleate boiling of binary mixtures: development of a heat transfer correlation," *JSME Int. J. Ser. B Fluids Therm. Eng.*, vol. 40, pp. 134–141, 1997. DOI: [10.1299/jsmeb.40.134](https://doi.org/10.1299/jsmeb.40.134).
- [26] Y. Fujita and M. Tsutsui, "Experimental investigation in pool boiling heat transfer of ternary mixture and heat transfer correlation," *Exp. Therm. Fluid Sci.*, vol. 26, pp. 237–244, 2002. DOI: [10.1016/S0894-1777\(02\)00132-2](https://doi.org/10.1016/S0894-1777(02)00132-2).
- [27] E. Meléndez and R. Reyes, "The pool boiling heat transfer enhancement from experiments with binary mixtures and porous heating covers," *Exp. Therm. Fluid Sci.*, vol. 30, pp. 185–192, 2006. DOI: [10.1016/j.expthermfluidsci.2005.05.005](https://doi.org/10.1016/j.expthermfluidsci.2005.05.005).
- [28] K. Armijo and V. Carey, "Prediction of binary mixture boiling heat transfer in systems with strong Marangoni effects," *Front. Heat Mass Transfer*, vol. 1, pp. 1–6, 2010.
- [29] T. Inoue, Y. Teruya, and M. Monde, "Enhancement of pool boiling heat transfer in water and ethanol/water mixtures with surface-active agent," *Int. J. Heat Mass Transfer*, vol. 47, pp. 5555–5563, 2004. DOI: [10.1016/j.ijheatmasstransfer.2004.05.037](https://doi.org/10.1016/j.ijheatmasstransfer.2004.05.037).
- [30] A. K. Dewangan, A. Kumar, and R. Kumar, "Pool boiling of iso-butane and quasi azeotropic refrigerant mixture on coated surfaces," *Exp. Therm. Fluid Sci.*, vol. 85, pp. 176–188, 2017. DOI: [10.1016/j.expthermfluidsci.2017.02.028](https://doi.org/10.1016/j.expthermfluidsci.2017.02.028).
- [31] Y. Im, C. Dietz, S. S. Lee, and Y. Joshi, "Flower-like CuO nanostructures for enhanced boiling," *Nanoscale Microscale Thermophys. Eng.*, vol. 16, pp. 145–153, 2012. DOI: [10.1080/15567265.2012.678564](https://doi.org/10.1080/15567265.2012.678564).
- [32] S. U. Ilyas, R. Pendyala, and N. Marneni, "Stability and agglomeration of alumina nanoparticles in ethanol-water mixtures," *Procedia Eng.*, vol. 148, pp. 290–297, 2016. DOI: [10.1016/j.proeng.2016.06.616](https://doi.org/10.1016/j.proeng.2016.06.616).
- [33] W.-T. Ji, P.-F. Zhao, C.-Y. Zhao, J. Ding, and W.-Q. Tao, "Pool boiling heat transfer of water and nanofluid outside the surface with higher roughness and different wettability," *Nanoscale Microscale Thermophys. Eng.*, vol. 22, pp. 296–323, 2018. DOI: [10.1080/15567265.2018.1497110](https://doi.org/10.1080/15567265.2018.1497110).
- [34] C. S. Sujith Kumar, Y. W. Chang, and P.-H. Chen, "Effect of heterogeneous wettable structures on pool boiling performance of cylindrical copper surfaces," *Appl. Therm. Eng.*, vol. 127, pp. 1184–1193, 2017. DOI: [10.1016/j.applthermaleng.2017.08.069](https://doi.org/10.1016/j.applthermaleng.2017.08.069).
- [35] M. Zupančič, M. Može, P. Gregorčič, and I. Golobič, "Nanosecond laser texturing of uniformly and non-uniformly wettable micro structured metal surfaces for enhanced boiling heat transfer," *Appl. Surf. Sci.*, vol. 399, pp. 480–490, 2017. DOI: [10.1016/j.apsusc.2016.12.120](https://doi.org/10.1016/j.apsusc.2016.12.120).
- [36] B. Shen, *et al.* "Enhanced pool boiling of ethanol on wettability-patterned surfaces," *Appl. Therm. Eng.*, vol. 149, pp. 325–331, 2019. DOI: [10.1016/j.applthermaleng.2018.12.049](https://doi.org/10.1016/j.applthermaleng.2018.12.049).
- [37] R. P. Sahu, S. Sinha-Ray, S. Sinha-Ray, and A. L. Yarin, "Pool boiling on nano-textured surfaces comprised of electrically-assisted supersonically solution-blown, copper-plated nanofibers: experiments and theory," *Int. J. Heat Mass Transfer*, vol. 87, pp. 521–535, 2015. DOI: [10.1016/j.ijheatmasstransfer.2015.04.009](https://doi.org/10.1016/j.ijheatmasstransfer.2015.04.009).

- [38] A. Sankaran, W. Zhang, and A. L. Yarin, “Pool boiling in deep and shallow vessels and the effect of surface nano-texture and self-rewetting,” *Int. J. Heat Mass Transfer*, vol. 127, pp. 857–866, 2018. DOI: [10.1016/j.ijheatmasstransfer.2018.08.046](https://doi.org/10.1016/j.ijheatmasstransfer.2018.08.046).
- [39] M. M. Rahman, J. Pollack, and M. McCarthy, “Increasing boiling heat transfer using low conductivity materials,” *Sci. Rep.*, vol. 5, pp. 13145, 2015. DOI: [10.1038/srep13145](https://doi.org/10.1038/srep13145).
- [40] J. Voglar, P. Gregorčič, M. Zupančič, and I. Golobič, “Boiling performance on surfaces with capillary-length-spaced one- and two-dimensional laser-textured patterns,” *Int. J. Heat Mass Transfer*, vol. 127, pp. 1188–1196, 2018. DOI: [10.1016/j.ijheatmasstransfer.2018.07.056](https://doi.org/10.1016/j.ijheatmasstransfer.2018.07.056).
- [41] P. Gregorčič, M. Zupančič, and I. Golobič, “Scalable surface microstructuring by a fiber laser for controlled nucleate boiling performance of high- and low-surface-tension fluids,” *Sci. Rep.*, vol. 8, pp. 7461, 2018. DOI: [10.1038/s41598-018-25843-5](https://doi.org/10.1038/s41598-018-25843-5).
- [42] Y. Y. Hsu, “On the size range of active nucleation cavities on a heating surface,” *J. Heat Transfer*, vol. 84, pp. 207–213, 1962. DOI: [10.1115/1.3684339](https://doi.org/10.1115/1.3684339).
- [43] E. W. Lemmon, I. H. Bell, M. L. Huber, and M. O. McLinden, “NIST standard reference database 23: reference fluid thermodynamic and transport properties-REFPROP, Version 10.0, Nat. Inst. Stand. Technol., Stand. Reference Data Program, Gaithersburg, 2018.
- [44] I. Golobič and M. Zupančič, “Wall-temperature distributions of nucleate pool boiling surfaces vs. boiling curves: A new approach,” *Int. J. Heat Mass Transfer*, vol. 99, pp. 541–547, 2016. DOI: [10.1016/j.ijheatmasstransfer.2016.04.033](https://doi.org/10.1016/j.ijheatmasstransfer.2016.04.033).
- [45] L. Zhang, J. H. Seong, and M. Bucci, “Percolative scale-free behavior in the boiling crisis,” *Phys. Rev. Lett.*, vol. 122, pp. 134501, 2019. DOI: [10.1103/PhysRevLett.122.134501](https://doi.org/10.1103/PhysRevLett.122.134501).

Supplementary Material for

Investigation of nucleate pool boiling of saturated pure liquids and ethanol - water mixtures on smooth and laser-textured surfaces

Peter Zakšek^a, Matevž Zupančič^{b*}, Peter Gregorčič^b, Iztok Golobič^b

^a Krško Nuclear Power Plant, Vrbina 12, SI-8270 Krško, Slovenia

^b Faculty of Mechanical Engineering, University of Ljubljana, Aškerčeva 6, SI-1000 Ljubljana, Slovenia

**matevz.zupancic@fs.uni-lj.si*

Pool boiling experimental setup

The experimental setup for the saturated pool boiling experiments consists of a $170 \times 100 \times 100 \text{ mm}^3$ pool boiling chamber made of double-pane glass and steel plates on the top and the bottom of the chamber, as shown in Fig. S1b [S1]. The heater unit is mounted on the bottom of the chamber and consists of a ceramic base with two electrical contacts to hold and power the stainless steel foil with a size of $27 \times 17 \text{ mm}^2$ (Fig. S1a). The ceramic base has a $23 \times 13 \text{ mm}^2$ borehole milled in the center to enable recording of the transient temperature fields on the bottom side of the foil. A golden mirror is placed below the heater at an angle of 45° to reflect the thermal radiation to the IR camera.

The vaporized working fluid condenses on the top and returns to the boiling chamber so that its level is maintained approximately 3.5 cm above the boiling surface. Immersed cartridge heaters are used for preheating, degassing and maintaining saturation conditions. The metal foil is heated using the Joule effect and the heat flux equals to the product of the current and the voltage drop across the foil, divided by its surface area. A homogenous heat generation across the foil is assumed.

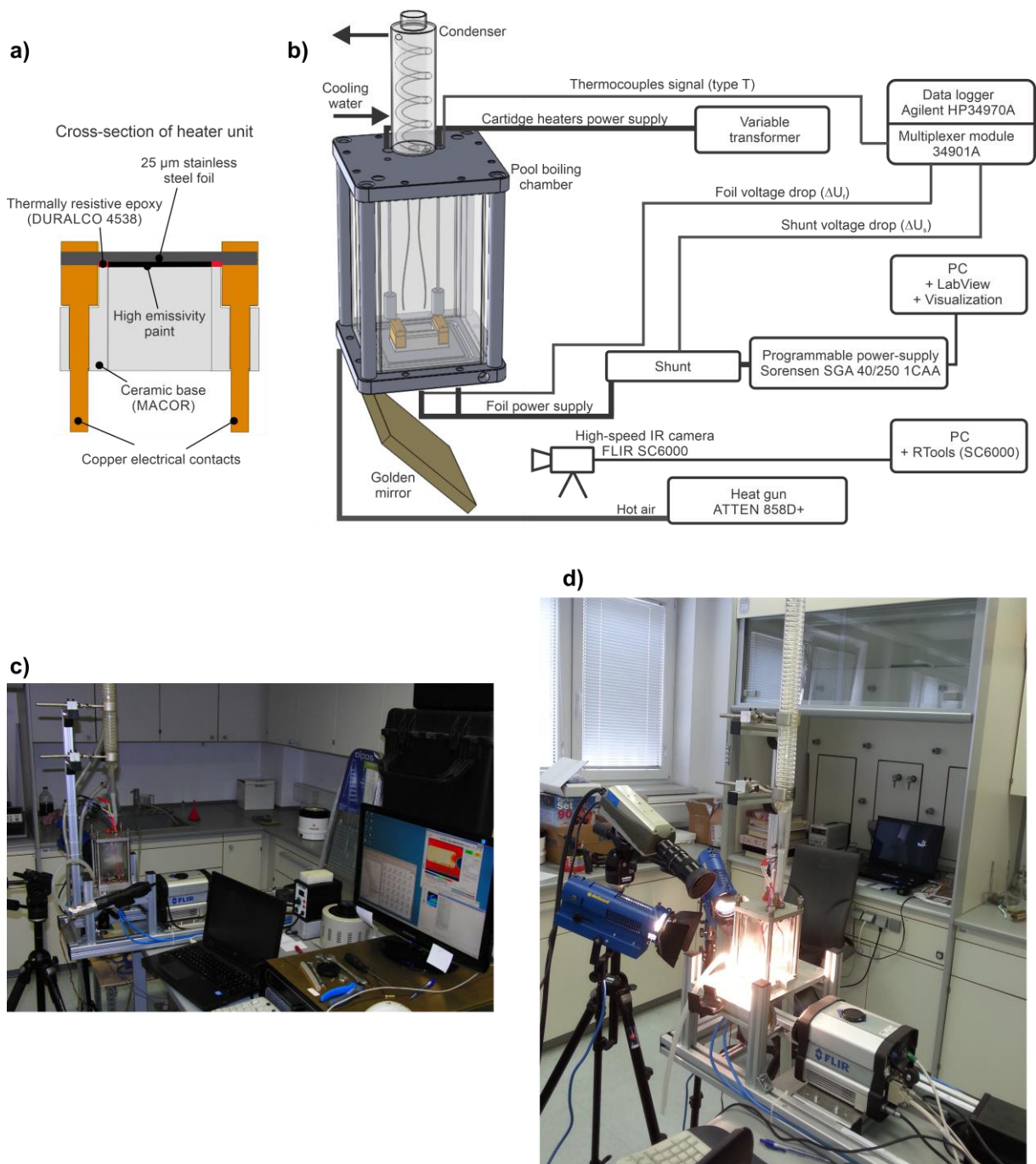


Figure S1. a) Cross-section of the thin-metal-foil heater unit; b) pool boiling experimental setup [S1]; c)-d) photos of the pool-boiling experimental setup.

Uncertainty of the IR temperature measurement

A high-speed IR camera (FLIC SC6000) was used to record the transient temperature field on the bottom of the stainless steel foils during the pool boiling experiments with a frame rate of 1000 fps and a spatial resolution of $250 \mu\text{m pixel}^{-1}$. The conversion from the raw digitalized IR signal into temperature was done using a calibration curve obtained under the same ambient conditions as were later maintained during the actual boiling experiments. The absolute expanded uncertainty of the temperature measurement is determined to be around 2 K and was practically constant across the entire calibration range (80–180 °C). However, the noise equivalent differential temperature (i.e., sensitivity) of the IR sensor is 20 mK. The uncertainty of the temperature difference among the individual pixels is therefore much lower than the absolute temperature uncertainty.

Uncertainty of the heat flux and the heat transfer coefficient

The expanded relative measurement uncertainty of the heat flux is estimated to be 0.5% of the heat flux. This results from the combined measurement uncertainty of the voltage drop across the foil, the electrical current and the uncertainty of the heater area. The uncertainty of the heat transfer coefficient depends on the inaccuracies in the heat flux and wall-temperature measurements. The maximum expanded uncertainty of the heat transfer coefficient equals $3.5 \text{ kW m}^{-2} \text{ K}^{-1}$, which can be greater than 100% of the value at the low heat fluxes and low superheats. However, the relative uncertainty decreases as the superheat and the heat flux increase.

Heat conduction through the heater

Vertical heat conduction under the steady state conditions

The stainless steel foils were painted on the bottom side with a high emissivity paint to improve the IR thermography measurements. The paint consisted of 40% silicone-polyester binder and 60% amorphous carbon (Pigment Black 7). The physical properties of the stainless steel and the paint are listed in Table S1. The average spectral emissivity of the paint was measured to be 0.9 in the mid-wave infrared band (3 to 5 μm).

Table S1. Material properties of the stainless steel foil and the high emissivity paint.

Material	Thickness δ (μm)	Density ρ (kg/m^3)	Specific heat c_p (kJ/kgK)	Thermal conductivity k (W/mK)
Stainless steel, S316	25	7990	0.50	16.2
High emissivity paint	5	1560	0.95	78.0

Since the boiling occurred on top of the foils and the temperature fields were on the bottom, we estimated the steady state heat conduction through the entire heater, as schematically presented in Fig. S2. We should note that laser processing, that is performed on the stainless steel foils, does not require any additional surface treatment/coating and therefore we presume it does not increase thermal resistance of the heater.

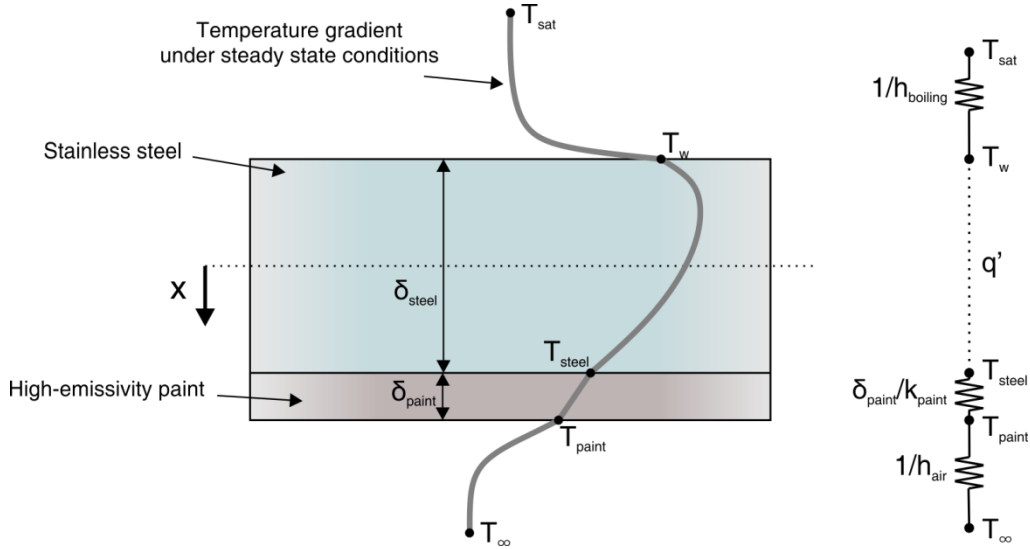


Figure S2. The vertical heat conduction through the heater. Schematic representation of the one-dimensional, steady state, heat transfer profile in the stainless steel foil and high emissivity paint.

The heat flux through the high emissivity paint equals

$$q_{paint} = -\frac{k_{paint}}{\delta_{paint}}(T_{paint} - T_{steel}) = h_{air}(T_{paint} - T_{\infty}), \quad (S1)$$

where k , h and δ denote the thermal conductivity, the heat transfer coefficient and the material thickness, respectively. The surrounding temperature (T_{∞}) was kept constant during the experiments at 25 °C.

Based on the McAdams' correlation [S2] for the natural convection from a down-facing horizontal plate, the convective heat transfer coefficient between the bottom heater surface and the air is around 10 W/m²K for a heater temperature in the range 100–300 °C. The temperature gradient across the stainless steel foil was determined by solving the steady state, heat conduction equation with internal thermal energy generation (q')

$$\frac{d^2T}{dx^2} + \frac{q'}{k_{steel}} = 0 . \quad (S2)$$

The boundary conditions for our example are

$$\begin{aligned} T|_{x=\delta_{steel}/2} &= T_{steel} \\ T|_{x=-\delta_{steel}/2} &= T_w \\ k_{steel} \frac{dT}{dx} \Big|_{x=-\delta_{steel}/2} &= h_{boiling} (T_w - T_{sat}) = q' \delta_{steel} - q_{paint} \end{aligned} \quad (S3)$$

Considering the first two boundary conditions in Eq. (S3), the solution to the differential equation is

$$T(x) = -\frac{q'}{2k_{steel}} \left(\left(\frac{\delta_{steel}}{2} \right)^2 - x^2 \right) + (T_{steel} - T_w) \frac{x}{\delta_{steel}} + \frac{T_{steel} + T_w}{2} . \quad (S4)$$

Taking into account the third boundary condition in Eq. (S3), we can calculate the temperature difference between T_{steel} and T_w as

$$T_{steel} - T_w = \left(q' \frac{\delta_{steel}}{2} - q_{paint} \right) \frac{\delta_{steel}}{k_{steel}} . \quad (S5)$$

The effect of the steady state heat conduction through the heater was evaluated for the highest heat flux ever reported on the 25-micron foils, which was around 1400 kW m⁻² during boiling on a superhydrophilic surface [S1]. This corresponds to a thermal energy generation rate of 56 GW m⁻³. At this point, the measured temperature on the surface of the high emissivity paint equaled 141 °C. Based on Eq. (S1), the heat flux to the air is around 1.2 kW m⁻², which is less than 0.1% of the electrically generated heat flux. In fact, the calculated heat loss is an overestimate, since the actual heat transfer coefficient is lower due to the stagnant air under the foil, which is held in the rectangular borehole in the test section. Most of the heat is, therefore,

removed by the working fluid and the heat losses through the bottom were neglected in our analysis. The temperature difference between the bottom of the heater (T_{paint}) and the wall temperature (T_{wall}) is calculated to be around 1.1 K. This value is still within the uncertainty of the IR temperature measurement (2 K).

Heater response to a periodic temperature disturbance

The bubbles at one nucleation site nucleate with a certain frequency that is relatively constant for a given heat flux. The nucleation occurs at a certain wall superheat and the surface rapidly cools down during the bubble's growth. After the bubble's departure, the surface heats up again until the next nucleation occurs. If we consider the temperature disturbance on the surface as a harmonic function, we can calculate the transient temperature distribution along the thickness of the heater. The one-dimensional transient heat conduction equation is

$$\frac{\partial^2 T}{\partial x^2} = \frac{1}{a} \frac{\partial T}{\partial t} , \quad (S6)$$

where a denotes the thermal diffusivity. We consider the heater as an infinite medium and the boundary conditions for a given example (see Fig. S3) are given by

$$\begin{aligned} T(0, t) &= T_w + \Delta T_w \left(e^{i2\pi f_b t} \right) \\ T(\infty, t) &= T_w \end{aligned} , \quad (S7)$$

where f_b is the nucleation frequency, T_w is the average wall temperature at a certain operating point and ΔT_w is the amplitude of the harmonic temperature disturbance. The result of Eq. (S6) is

$$T(x, t) = T_w + \Delta T_w e^{-\sqrt{\pi f_b / a} x} e^{-i\sqrt{\pi f_b / a} (x - \sqrt{4\pi f_b a} t)} . \quad (S8)$$

We evaluated the transient heat conduction through the 25- μm -thick stainless steel foil and 5- μm -thick high emissivity paint for nucleation frequency of 90 Hz and surface temperature of 118 $^{\circ}\text{C}$, where the maximum amplitude of the temperature disturbance was 10 $^{\circ}\text{C}$. These parameters were previously recorded during our studies on boiling of water on biphilic surfaces [S1]. The results, given in Fig. S3b, show that the heat conduction through the high emissivity paint is negligible, but could be important for the stainless steel layer. In the worst case, the temperature difference between the top of the stainless steel foil and the bottom of the paint is 2 K. This suggests that the actual measurement uncertainty could be more than 2 K in some cases. During boiling of pure ethanol, where bubbles are relatively small and nucleate with a high frequency, the limited thermal response of the heater also limits the applicability of the IR thermography.

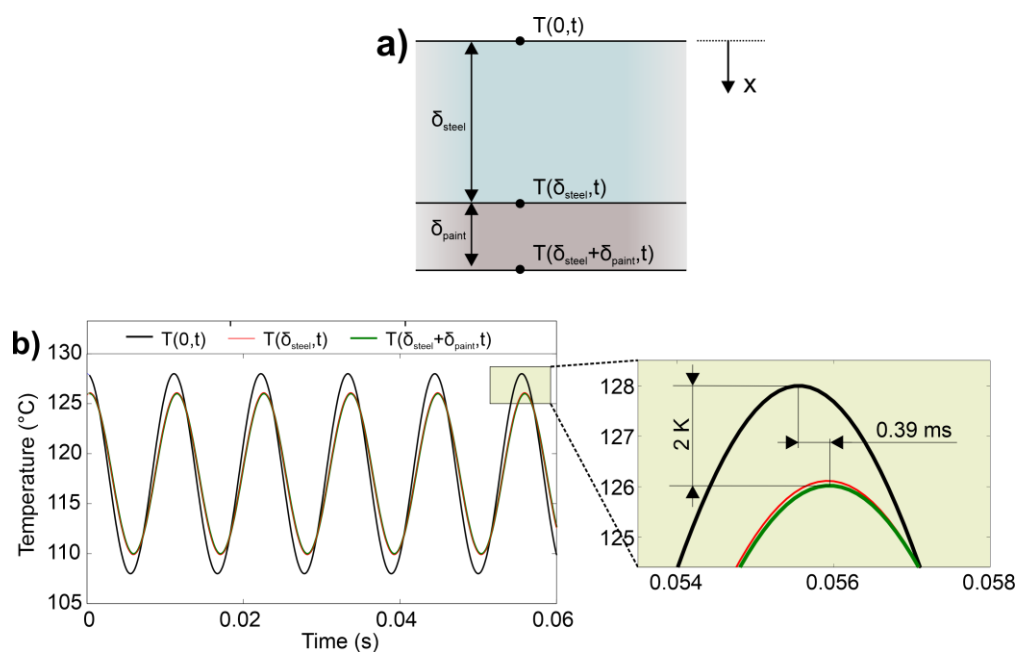


Figure S3. a) A schematic representation of the heater and b) thermal response of a stainless steel foil and high emissivity paint to a harmonic temperature disturbance.

Effect of lateral heat conduction

The results of our experiments are spatio-temporal temperature fields of the boiling surface. It is therefore possible to estimate the local heat transfer coefficient and the local heat flux for every pixel of the measured temperature field. This could be done by solving the inverse heat conduction problem [S3, S4] or by using the energy-balance-based equation [S5] for the local heat transfer coefficient and the local heat flux

$$h^N(x, y) = \frac{1}{2} \left\{ \begin{array}{l} \frac{q_{in} - \delta\rho c_p \frac{T_w^{N+1}(x, y) - T_w^N(x, y)}{\Delta t} + \delta k \left(\frac{\partial^2 T_w^N(x, y)}{\partial x^2} + \frac{\partial^2 T_w^N(x, y)}{\partial y^2} \right)}{T_w^N(x, y) - T_{sat}} + \\ \frac{q_{in} - \delta\rho c_p \frac{T_w^{N+1}(x, y) - T_w^N(x, y)}{\Delta t} + \delta k \left(\frac{\partial^2 T_w^{N+1}(x, y)}{\partial x^2} + \frac{\partial^2 T_w^{N+1}(x, y)}{\partial y^2} \right)}{T_w^{N+1}(x, y) - T_{sat}} \end{array} \right\}, \quad (S9)$$

$$q^N(x, y) = h(x, y) \left(\frac{T_w^{N+1} + T_w^N}{2} - T_{sat} \right). \quad (S10)$$

The subscripts N and $N+1$ indicate two consecutive time points and q_{in} is equal to the electrically generated input heat flux. The use of a time-averaged wall temperature $(T^{N+1} + T^N)/2$ only leads to small apparent inconsistencies between the plots of T^N , q^N and h^N when the temperature is changing very rapidly in the first 1–2 ms. To evaluate the effect of lateral thermal conduction in the heater, the calculations were performed with and without the lateral conduction terms in Eq. (S9). All the calculations were performed only for the stainless steel layer, since we already proved that high emissivity paint has a negligible effect on the heat transfer and the temperature distribution across the heater. The results in Fig. S4 show that lateral conduction has a low impact on the local heat flux and the local heat transfer coefficient, which is mainly due to the small thickness and the low thermal capacity of the heated foil. Some difference between the values calculated with and without the lateral conduction terms could be observed at points that are subjected to the highest temperature changes (i.e., the middle of

the nucleation site). However, the relative difference between the values is on average less than 1%. Lateral conduction, therefore, only negligibly affects the spatial resolution and the uncertainty of the temperature measurement.

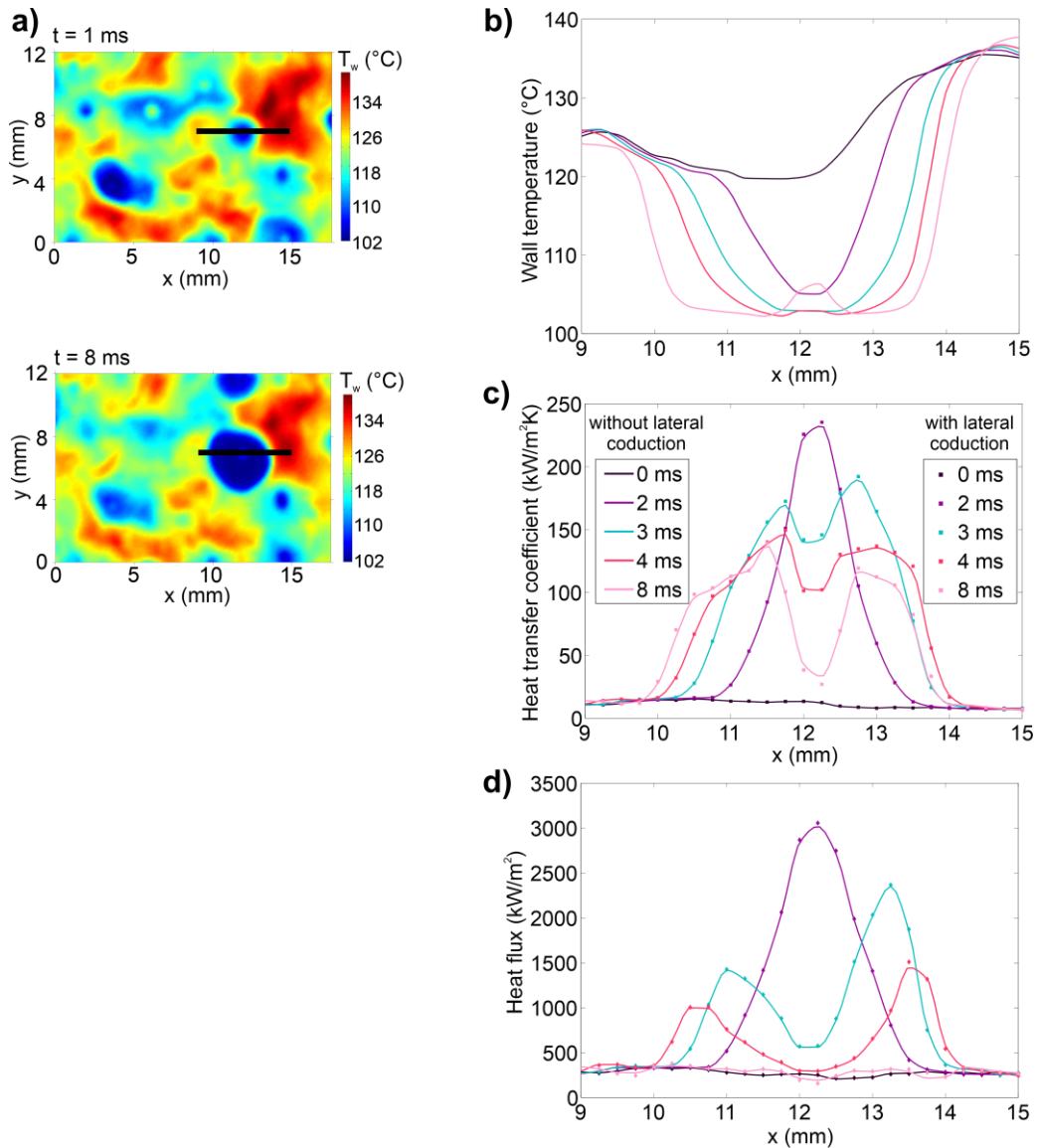


Figure S4. a) An example of the temperature field during boiling of pure water on a stainless steel foil at the beginning of the nucleation (1 ms) and after the end of the bubble's growth (8 ms). Black lines indicate the cut-off section of the temperature profiles. b) Temperature profiles across the nucleating bubble during bubble growth. c) Local heat transfer coefficient during bubble growth across the profile marked in a). Square-like symbols and continuous lines represent the values with and without accounting for the lateral thermal conduction, respectively. d) Local heat flux during bubble growth; diamond-like symbols and continuous lines represent the values with and without accounting for the lateral thermal conduction, respectively.

Surface roughness of smooth and laser-textured samples

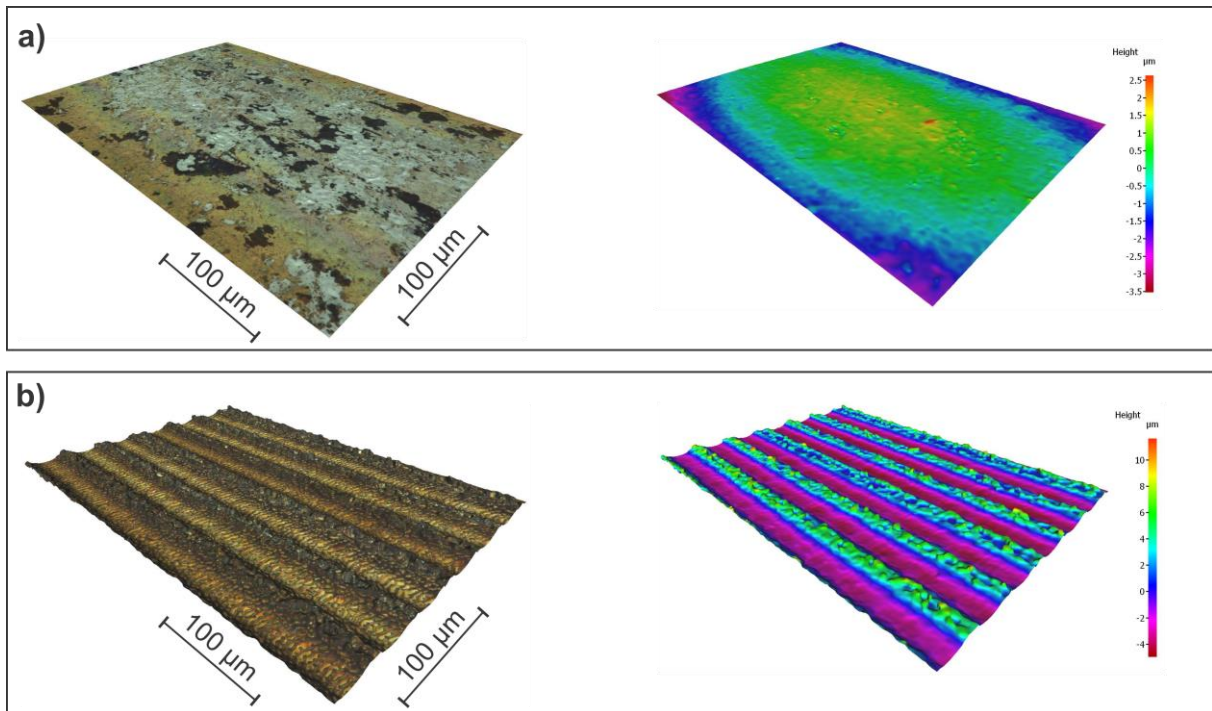


Figure S5. Surface topography images obtained by an optical confocal microscope (Alicona InfiniteFocus, 50x magnification) for a) smooth (unprocessed) stainless steel and b) laser-textured region. Results were obtained on a surface with laser pattern width equal to 2.0 mm ($P = 2.5$ mm) and completely comparable values were also measured on all other laser-textured foils.

References

- S1. Zupančič, M., et al., *Enhanced pool-boiling heat transfer on laser-made hydrophobic/superhydrophilic polydimethylsiloxane-silica patterned surfaces*. Applied Thermal Engineering, 2015. **91**: p. 288-297.
- S2. McAdams, W.H., *Heat Transmission*. 3rd edition ed. 1954, New York: McGraw-Hill Book Company.
- S3. Heng, Y., et al., *Estimation of local nucleate boiling heat flux using a three-dimensional transient heat conduction model*. Inverse Problems in Science and Engineering, 2010. **18**(2): p. 279-294.
- S4. Petkovsek, J., et al., *IR thermographic investigation of nucleate pool boiling at high heat flux*. International Journal of Refrigeration, 2016. **61**: p. 127-139.
- S5. Golobic, I., et al., *Experimental determination of transient wall temperature distributions close to growing vapor bubbles*. Heat and Mass Transfer, 2009. **45**(7): p. 857-866.